JOURNAL OF COMPUTATIONAL PHYSICS 105, 252–266 (1993)

A Triangle Based Mixed Finite Element—Finite Volume Technique for Modeling Two Phase Flow through Porous Media

LOUIS J. DURLOFSKY

Chevron Oil Field Research Company, P.O. Box 446, La Habra, California 90633-0446

Received April 27, 1992; revised August 5, 1992

Triangle based discretization techniques offer great advantages relative to standard finite difference methods for the modeling of flow through geometrically complex geological features. The purpose of this paper is to develop and apply a triangle based method for the modeling of two phase flow through porous formations. The formulation includes the effects of gravity, compressibility, and capillary pressure. The technique entails a triangle based mixed finite element method for solution of the variable coefficient, parabolic pressure equation, and a second-order TVD-type (total variation diminishing) finite volume scheme for solution of the essentially hyperbolic saturation equation. The method is applied to a variety of example problems and is shown to perform very well on problems involving geometric complexity coupled with heterogeneous, generally anisotropic permeability descriptions.

1. INTRODUCTION

Geometrically complex geological structures, such as faults, cross stratified beddings and large scale inclined strata, can have profound effects on the flow of fluids through subsurface formations. Standard finite difference methodology, typically used for oil reservoir simulation, lacks the geometric flexibility required for modeling flow through or around such structures. Triangle based discretization methods, by contrast, offer an attractive means to discretize and simulate flow through complex strata. The development, implementation, and application of such a scheme is the subject of this paper.

The equations governing immiscible displacement in porous media can be expressed in terms of two coupled equations, the pressure equation and the saturation equation. The pressure equation, which describes the pressure field throughout the formation, is in general a variable coefficient parabolic partial differential equation. The saturation equation, which describes the saturations (volume fractions) of fluids throughout the reservoir, is an essentially hyperbolic conservation law (capillary pressure effects introduce small dispersion-like terms). The accurate numerical solution of these two equations is complicated by several factors. Permeability, which enters the formulation through the coefficients in the pressure equation, is a full tensor quantity that is often extremely variable over very short distances. This results in the appearance of highly discontinuous coefficients in the discretized pressure equation. Additional difficulties can arise because the velocity field, required for solution of the saturation equation, is determined from Darcy's law via differentiation of the pressure field and multiplication by the discontinuous permeability coefficients. Many numerical approaches, such as standard Galerkin finite element procedures, are not very well suited for such calculations and can yield inaccurate velocity fields that are not continuous across element edges. Finally, because the saturation equation is essentially hyperbolic in character, numerical dispersion can act to seriously degrade numerical solutions if inaccurate solution techniques are used.

The purpose of this paper is to present an accurate triangle based method for the modeling of two phase flow through porous media. The effects of gravity, capillary pressure and compressibility are included. The formulation is for two dimensional systems but the general approach can be applied in three dimensions as well. The method is formulated to handle generally anisotropic, highly discontinuous permeability fields, yield accurate velocity fields and minimize numerical dispersion. The pressure equation is solved via a mixed finite element method such as that used in [1, 2]. Mixed methods are particularly well suited to problems with highly discontinuous coefficients and to those where the secondary or flux variable (integrals of velocity through element edges) is required to a degree of accuracy comparable to that of the primary variable (pressure). This is accomplished by approximating the two fields individually, as will be seen in Section 2.

The saturation equation is solved with a second-order triangle based TVD-type finite volume scheme. TVD (total variation diminishing) schemes are a class of second-order accurate methods that eliminate spurious oscillations in the numerical solutions of hyperbolic conservation laws. The basic finite volume method applied in this study was originally presented in [3] and further refined in [4]. The

0021-9991/93 $5.00

scheme minimizes numerical dispersion relative to a first-order method and is particularly well suited for coupling with the velocity field computed via the mixed finite element solution of the pressure equation. This is because the finite volume scheme directly utilizes integrals of fluxes through element edges, which are known very accurately from the mixed finite element solution. More specifically, for the lowest order mixed method applied in this study, these fluxes are superconvergent and are therefore computed to $O(l^2)$ accuracy, where l is a typical element side length. The overall method therefore combines a continuous, second-order approximation for the velocity field with a second-order TVD-type scheme for solution of the saturation equation.

Previous investigators have developed triangle based methods to model immiscible displacements in porous media. The method developed in the present study most closely resembles the general formulations of [1, 2], which utilized a mixed finite element method for solution of the pressure equation and a discontinuous finite element method for solution of the saturation equation. These formulations were for incompressible systems, while the formulation presented here is for compressible systems. The discontinuous finite element method used in [1, 2] for solution of the saturation equation is a two-step procedure which requires the calculation of three saturation values in each triangular element. In addition, the slope limiting procedure applied in [1, 2] requires the solution of local optimization problems for each element. The finite volume method applied in this study for solution of the saturation equation is simpler and more efficient than the discontinuous finite element method of [1, 2]. This is because the scheme requires only a single unknown in each element (rather than three) and utilizes a slope limiting procedure that is quite straightforward to implement. Some recent discontinuous finite element schemes [5, 6], which extend the earlier approaches, are also potentially applicable to the solution of the saturation equation.

Other methods applicable to the solution of two phase flow through geometrically complex porous media include the control volume finite element methods presented in, for example, [7, 8]. These methods have the advantage that they can be fairly readily introduced into current finite difference reservoir simulators. However, the control volume finite element methods are based on a Galerkin finite element approach for the pressure equation and a first-order accurate upwinding of the saturation equation. Neither of these treatments achieves the accuracy of the approaches presented in this paper. The Galerkin finite element method does not optimally weight the mobilities and does not yield continuous velocities across element edges. This problem is circumvented in the control volume finite element approach by defining control volumes, which essentially comprise an auxiliary grid. Velocities computed on this auxiliary grid are continuous, but their accuracy is not of the level attained by mixed finite element methods.

Finally, the mixed finite element-modified method of characteristics approaches developed for rectangular elements by, among others, [9, 10], could be extended to triangular elements. This approach may lose some accuracy for triangular elements relative to rectangular elements because fluxes, rather than the velocities required for the solution of the saturation equation via a modified method of characteristics, are computed accurately via a triangle based mixed finite element method. This may lead to mass conservation problems in the solution of the saturation equation.

This paper proceeds as follows. The governing equations and numerical formulation for the modeling of two phase flow through porous media are presented in Section 2. The mixed finite element method for solution of the pressure equation and the higher order finite volume method for solution of the saturation equation are discussed in detail. Examples demonstrating the applicability and strengths of the method for the modeling of flow through complex geological structures are presented in Section 3. Conclusions and future directions are discussed in Section 4.

2. GOVERNING EQUATIONS AND NUMERICAL FORMULATION

In this section we formulate the equations governing slightly compressible, two phase immiscible displacements in two dimensions. Gravity and capillary pressure effects are included. Next, the mixed finite element method applied to the solution of the pressure equation and the higher order finite volume method for solution of the saturation equation are presented in detail. Examples demonstrating the individual performances of both the mixed finite element method and the higher order finite volume method are provided.

2.1. *Equations for Immiscible Displacement*

The equations describing two phase immiscible displacement in porous media can be derived by combining Darcy's law, written for each phase individually, with conservation of mass for each phase. These equations can be readily manipulated (see [11] for details) into a parabolic equation describing the pressure field throughout the reservoir (the pressure equation) and an essentially hyperbolic equation describing the propagation of fluid fronts through the reservoir (the saturation equation):

$$\nabla \cdot [(\mathbf{m}_w + \mathbf{m}_o) \cdot \nabla p] + \frac{1}{2} \nabla \cdot [(\mathbf{m}_o - \mathbf{m}_w) \cdot \nabla p_c] - g \nabla \cdot [(\mathbf{m}_o \rho_o + \mathbf{m}_w \rho_w) \cdot \nabla D] + Q_t = \phi c_t \frac{\partial p}{\partial t}, \quad (1a)$$

$$\nabla \cdot (\mathbf{h}_w \cdot \nabla S_w) - \nabla \cdot (f_w \mathbf{v}_t) - \nabla \cdot (\mathbf{G}_w \cdot \nabla D) + Q_w = \phi \frac{\partial S_w}{\partial t}, \quad (1b)$$

where the subscript w refers to the water phase and o to the oil phase. In the above, $\mathbf{m}_w$ is the mobility of the water, defined as

$$\mathbf{m}_w = \mathbf{k}\frac{k_{rw}}{\mu_w}, \tag{1c}$$

where $\mathbf{k}$ is the position-dependent absolute permeability tensor, k_{rw} is the water relative permeability, and μ_w is the water viscosity; $\mathbf{m}_o$, the mobility of the oil, is defined analogously. In Eq. (1a), the pressure equation, p is the average pressure of the water and oil phases, defined as $p = (p_w + p_o)/2$, p_c is capillary pressure, defined as $p_c = p_o - p_w$, ρ is density, g is the acceleration due to gravity, D is depth, Q_t is the total volumetric injection rate, Q_w is the water injection rate, ϕ is porosity, c_t is the total compressibility of the rock–fluid system, and t is time. In Eq. (1b), the saturation equation,

$$\mathbf{h}_w = -\mathbf{m}_o f_w \frac{dp_c}{dS_w}, \tag{1d}$$

where f_w is the fractional flow of water defined as

$$f_w = \frac{k_{rw}/\mu_w}{k_{rw}/\mu_w + k_{ro}/\mu_o}, \tag{1e}$$

S_w is the saturation, or volume fraction, of water, $\mathbf{v}_t$ is the total velocity of the system, defined as $\mathbf{v}_t = \mathbf{v}_w + \mathbf{v}_o$, and

$$\mathbf{G}_w = f_w(\rho_w - \rho_o)\, g\, \mathbf{m}_o. \tag{1f}$$

The equations above describe the two-phase flow of slightly compressible fluids through porous media. The only term accounting for the effects of compressibility is the time derivative in the pressure equation. The formulation is applicable to slightly compressible fluids because, in the derivation, terms of the form $c_t \mathbf{m} \cdot \nabla p \cdot \nabla p$ are neglected compared to terms of the form $\nabla \cdot \mathbf{m} \cdot \nabla p$. This approximation is justified when $c_t(\Delta p) \ll 1$, where Δp is the characteristic pressure drop through the system. For reservoir flow problems, Δp is typically $O(1000$ psi) and c_t, for reservoir liquids (oil and water), is about $10^{-6}\,\text{psi}^{-1}$. Thus, $c_t(\Delta p) \sim 10^{-3}$, and the requirement of slight compressibility is satisfied. For problems involving highly compressible fluids, this requirement may not be satisfied and the formulation adopted here may not be applicable. Also neglected in Eq. (1a) is the time derivative of the capillary pressure term, which is small compared to the time derivative of the average pressure.

Equations (1) can be nondimensionalized by identifying characteristic values for each variable. The resulting dimensionless equations are of identical form to those above. Two important dimensionless groups appear. The first, designated G_d, quantifies the ratio of gravitational effects to convective effects. It can be written as

$$G_d = \frac{k_c\, \Delta\rho g}{\mu_o v_c}, \tag{1g}$$

where k_c is the characteristic permeability (e.g., the geometric average of the element permeabilities), v_c is the characteristic total velocity, $\Delta\rho = \rho_w - \rho_o$, and the other variables are as defined previously. The second dimensionless group represents the ratio of convective terms to capillary pressure terms and can be thought of as a type of Peclet number. Designating this group Pe:

$$\text{Pe} = \frac{\mu_o v_c L}{\tilde{p}_c k_c}, \tag{1h}$$

where L is the characteristic length of the system and $\tilde{p}_c$ is the characteristic capillary pressure.

In the formulation discussed below, Eqs. (1) will be considered in the general forms presented above. At this point, however, we shall consider simplified versions of these equations which will enable us to better characterize the system. In general, the capillary pressure terms in the pressure equation are small compared to the average pressure terms. If we further neglect gravitational effects and the source term, Eq. (1a) simplifies to

$$\nabla \cdot [(\mathbf{m}_w + \mathbf{m}_o) \cdot \nabla p] = \phi c_t \frac{\partial p}{\partial t}. \tag{2a}$$

Capillary pressure effects are also typically small relative to the convective terms in Eq. (1b). Neglecting these terms, in addition to the source and gravity terms, gives

$$-\nabla \cdot (f_w \mathbf{v}_t) = \phi \frac{\partial S_w}{\partial t}. \tag{2b}$$

At this point the nature of the governing equations is apparent. Equation (2a) is a parabolic equation with position and saturation dependent coefficients. The saturation dependency of $\mathbf{m}_w$ and $\mathbf{m}_o$ renders them time dependent; their dependency on position ($\mathbf{x}$) results from the variation of both $\mathbf{k}$ and S_w in space. Due to the large magnitudes of variation in $\mathbf{k}$ with position, these coefficients are very discontinuous in $\mathbf{x}$. Equation (2b) is a nonlinear hyperbolic equation. The nonlinearity arises through the nonlinearity in f_w, which is typically a nonconvex function and is derived, in practice, from laboratory measurements. The additional terms in Eqs. (1) do not change the general nature of the equations but do complicate the formulation, as will be seen below.

The general solution procedure is as follows. An IMPES (implicit in pressure, explicit in saturation) type approach will be used to solve Eqs. (1). At the start of a time step, the pressure equation is solved implicitly via a backward Euler method and the pressure solution is advanced from time step n to time step $n+1$. The saturation field is held constant over this time step. As a result, the pressure solution at any time is linear; no Newton iterations are required. Following solution of the pressure equation, the total velocity $\mathbf{v}_t$ is known (this point is discussed in detail below), and the saturation equation can then be solved explicitly, with pressure and velocity (evaluated at time $n+1$) held constant over the time step. Due to the sequential treatment of the pressure and saturation equations, and the first-order accurate time discretization of the pressure equation, the global scheme is not formally second-order accurate in time. It can, however, be readily modified to achieve global second-order time accuracy, as discussed in Section 2.3, though this does not appear to be necessary in practice. We now consider the solution of the pressure equation.

2.2. *Mixed Finite Element Solution of the Pressure Equation*

As discussed in Section 1, mixed finite element methods are ideally suited to the solution of elliptic or parabolic equations with highly discontinuous coefficients, particularly when the flux or velocity field is also of interest. This is precisely the case in Eq. (1a) as the coefficients, through their dependency on $\mathbf{k}$, are highly discontinuous, and the coupling of Eqs. (1a) and (1b) is through $\mathbf{v}_t$. Therefore, a triangle based mixed finite element method will be applied to the solution of Eq. (1a).

In applying mixed finite element methods to the pressure equation, Eq. (1a) is not used directly. Rather, it is split into the two equations from which it is derived; conservation of mass and Darcy's law, as follows:

$$-\nabla\cdot\mathbf{v}_t + Q_t = \phi c_t \frac{\partial p}{\partial t}, \tag{3a}$$

$$\mathbf{v}_t = -(\mathbf{m}_w+\mathbf{m}_o)\cdot\nabla p - \tfrac{1}{2}(\mathbf{m}_o-\mathbf{m}_w)\cdot\nabla p_c + g(\mathbf{m}_o\rho_o+\mathbf{m}_w\rho_w)\cdot\nabla D. \tag{3b}$$

In the mixed finite element method, p and $\mathbf{v}_t$ are approximated separately. The approximation spaces for these variables are discussed in many references; see, e.g., [1]. The lowest order basis functions for p and $\mathbf{v}_t$, consistent with the requirements of the approximation spaces, are as follows: pressure is approximated via a basis function, designated Ψ^j, which is piecewise constant throughout the solution domain. The total velocity is approximated via a vector basis function $\mathbf{\Phi}^i$ whose normal component is continuous across the interfaces of adjacent elements. We designate the total number of elements in the domain M and the total number of element edges N. Then, the total velocity and pressure fields can be represented in terms of degrees of freedom α_i and β_j and basis functions $\mathbf{\Phi}^i$ and Ψ^j as

$$\mathbf{v}_t = \sum_{i=1}^{N} \alpha_i \mathbf{\Phi}^i, \tag{4a}$$

$$p = \sum_{j=1}^{M} \beta_j \Psi^j, \tag{4b}$$

where $\Psi^j = 1$ over element j and zero elsewhere and $\mathbf{\Phi}^i\cdot\mathbf{n}_j = \delta_{ij}$ (1 on edge i and zero elsewhere). The $\mathbf{\Phi}^i$ basis function is nonzero only over the two elements that share edge i.

The variational form of the pressure equation can now be expressed by weighting Eq. (3a) with the Ψ^k basis functions and Eq. (3b) with $\mathbf{\Phi}^k$, giving

$$-\int_\Omega (\nabla\cdot\mathbf{v}_t)\,\Psi^k\,dA + \int_\Omega Q_t\,\Psi^k\,dA = \int_\Omega \phi c_t \frac{\partial p}{\partial t}\,\Psi^k\,dA, \tag{5a}$$

$$\int_\Omega (\mathbf{m}_t^{-1}\cdot\mathbf{v}_t + \nabla p)\cdot\mathbf{\Phi}^k\,dA = \int_\Omega \left(-\frac{1}{2}(f_o-f_w)\nabla p_c + (\rho_o f_o+\rho_w f_w)\,g\,\nabla D\right)\cdot\mathbf{\Phi}^k\,dA, \tag{5b}$$

where $\mathbf{m}_t$ is the total mobility ($\mathbf{m}_t = \mathbf{m}_o+\mathbf{m}_w$) and f_o is the fractional flow of oil ($f_o = 1-f_w$). Introducing the approximations for p and $\mathbf{v}_t$ into Eqs. (5a) and (5b) and applying the divergence theorem yields, after some additional manipulation,

$$\alpha_i\int_\Omega (\nabla\cdot\mathbf{\Phi}^i)\,\Psi^k\,dA + \frac{d\beta_j}{dt}\int_\Omega \phi c_t \Psi^j\Psi^k\,dA = \int_\Omega Q_t\,\Psi^k\,dA, \tag{6a}$$

$$\alpha_i\int_\Omega (\mathbf{m}_t^{-1}\cdot\mathbf{\Phi}^i)\cdot\mathbf{\Phi}^k\,dA - \beta_j\int_\Omega (\nabla\cdot\mathbf{\Phi}^k)\,\Psi^j\,dA = -\int_{\partial\Omega} p_b(\mathbf{n}\cdot\mathbf{\Phi}^k)\,dl - \frac{1}{2}\int_\Omega (f_o-f_w)\times\left(\frac{dp_c}{dS_w}\right)\nabla S_w\cdot\mathbf{\Phi}^k\,dA + \int_\Omega (\rho_o f_o+\rho_w f_w)\,g\,\nabla D\cdot\mathbf{\Phi}^k\,dA, \tag{6b}$$

where the appearance of a repeated index indicates summation. Note that p_b in the integral over $\partial\Omega$ represents prescribed pressure boundary data. All terms on the right-hand sides of the above equations are considered known (i.e., functions of S_w only) when the pressure equation is solved: The approximation of the term involving dp_c/dS_w in Eq. (6b) will be discussed below in Section 2.3. To write Eq. (6a) in its final form, an approximation for $d\beta_j/dt$ is required. We shall approximate this term via a simple implicit Euler scheme; i.e.,

$$\frac{d\beta_j}{dt} = \frac{1}{\Delta t}(\beta_j^{n+1} - \beta_j^n), \tag{6c}$$

where the superscript indicates the time level and Δt the time step. Introducing this approximation into Eq. (6a) yields

$$\alpha_i \int_\Omega (\nabla \cdot \mathbf{\Phi}^i)\, \Psi^k \, dA + \frac{\beta_j^{n+1}}{\Delta t} \int_\Omega \phi c_t \Psi^j \Psi^k \, dA = \frac{\beta_j^n}{\Delta t} \int_\Omega \phi c_t \Psi^j \Psi^k \, dA + \int_\Omega Q_t \Psi^k \, dA, \tag{7}$$

where all terms on the RHS of Eq. (7) are known.

Equations (6b) and (7) represent a set of linear equations to be solved for the unknowns α_i and β_j. Upon evaluation of the integrals in Eqs. (6b) and (7) the following equation set results:

$$\begin{pmatrix} \mathbf{A} & \mathbf{B} \\ \mathbf{C} & \mathbf{D} \end{pmatrix} \begin{pmatrix} \alpha \\ \beta \end{pmatrix} = \begin{pmatrix} \mathbf{b}_1 \\ \mathbf{b}_2 \end{pmatrix}. \tag{8}$$

In the above, $\mathbf{A}$ is a square matrix of dimension N, $\mathbf{B}$ is a nonsquare matrix of dimension $N \times M$, $\mathbf{C}$, which is equal to $-\mathbf{B}^t$, is $M \times N$ and $\mathbf{D}$ is a square, diagonal matrix of dimension M. The $\mathbf{A}$ and $\mathbf{B}$ matrices are formed from the two terms on the LHS of Eq. (6b) and the $\mathbf{C}$ and $\mathbf{D}$ matrices are formed from the two terms on the LHS of Eq. (7). The $\mathbf{b}_1$ vector, of dimension N, contains terms from the RHS of Eq. (6b), while $\mathbf{b}_2$, of dimension M, contains terms from the RHS of Eq. (7). Each of the matrices in Eq. (8) is extremely sparse. The $\mathbf{A}$ matrix involves terms of the form $\mathbf{\Phi}^i \cdot \mathbf{\Phi}^k$. The $\mathbf{\Phi}^i$ basis function is nonzero only over the two elements containing edge i. Therefore, at most five nonzero entries can occur on a row in $\mathbf{A}$, regardless of how irregular the grid. The $\mathbf{B}$ and $\mathbf{C}$ matrices involve terms of the form $(\nabla \cdot \mathbf{\Phi}^i)\, \Psi^k$. Because Ψ^k is nonzero only in element k, the $\mathbf{B}$ matrix contains at most two nonzero terms per row and the $\mathbf{C}$ matrix at most three nonzero terms per row.

Note that pressure boundary conditions are enforced through the integral over $\partial\Omega$ appearing in the $\mathbf{b}_1$ vector. Flux boundary conditions are specified through adjustment of the appropriate terms in the $\mathbf{A}$ and $\mathbf{B}$ matrices to recover the desired α_i. Well terms (point sources and sinks) are not treated explicitly. Rather, a production index type approach, where a pressure difference between the well bore and the element centroid is specified, is utilized. More complex well models such as the sub-grid approach of [1, 2] could be used if the detailed modeling of near well bore behavior is required.

The linear solution of Eq. (8) can be accomplished through a variety of methods. Here, we rewrite the linear system in the form

$$(\mathbf{A} - \mathbf{B}\mathbf{D}^{-1}\mathbf{C})\alpha = \mathbf{b}_1 - \mathbf{B}\mathbf{D}^{-1}\mathbf{b}_2. \tag{9a}$$

This rearrangement is efficient computationally because $\mathbf{D}^{-1}$ is trivial to form ($\mathbf{D}$ is diagonal) and the matrix multiplications involve very sparse matrices. Also, due to the relationship between $\mathbf{B}$ and $\mathbf{C}$, the structure of the matrix $\mathbf{A} - \mathbf{B}\mathbf{D}^{-1}\mathbf{C}$ is identical to that of $\mathbf{A}$; i.e., no fill-in occurs. Thus, the matrix problem reduces to the solution of an order N system of linear equations, with at most five nonzero contributions per row. Equation (9a) can be solved using either direct or iterative (e.g., conjugate-gradient-like) methods. A direct method is used in the examples presented below. Once α is determined through solution of Eq. (9a), β can be readily computed through a multiplication as follows:

$$\beta = \mathbf{D}^{-1}(\mathbf{b}_2 - \mathbf{C}\alpha). \tag{9b}$$

At this point the pressure equation is fully solved and the pressure and velocity fields are known throughout the domain. The formulation yields both of these quantities to $O(l)$ accuracy, where l is the typical spacing between node points or, analogously, $l \sim (|\Delta|)^{1/2}$, where $|\Delta|$ is the area of a typical element. However, at certain points, superconvergence is obtained. Specifically, at element centroids, p is computed to $O(l^2)$ accuracy and, at edge midpoints (the Gauss points), $\mathbf{v}_t \cdot \mathbf{n}$ is likewise computed to $O(l^2)$ accuracy. This latter result is significant and will be exploited below in the solution of the saturation equation.

An alternate approach to the solution of the pressure equation exists for systems where the effects of compressibility, gravity and capillary pressure are negligible. In such cases, a nonconforming finite element formulation can be used for solution of the pressure equation; this method is equivalent to the mixed method when applied to such systems and yields identical results for centroid pressures and edge fluxes. For more discussion of the nonconforming finite element method and its equivalence with the mixed method, see [12].

This completes the description of the solution of the pressure equation. Before turning to the solution of the saturation equation, we consider a simple example problem

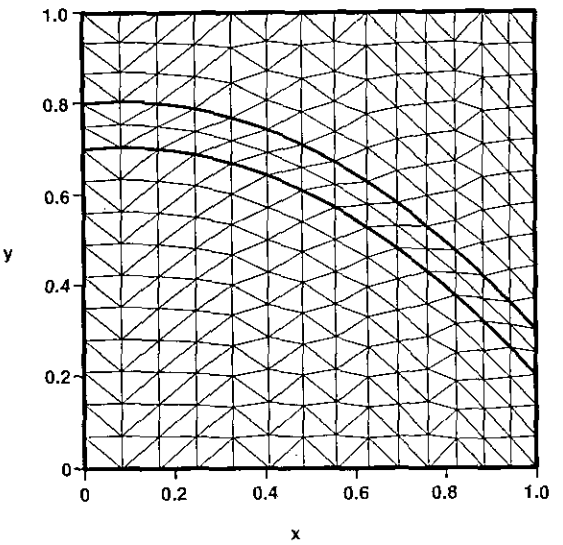

FIG. 1. Finite element mesh with low permeability streak.

which illustrates some of the strengths of the mixed finite element method. The finite element grid for this example is shown in Fig. 1. The problem to be solved involves single phase, steady state flow with no gravity effects (i.e., solution of Eq. (2a) with $\mathbf{m}_o = 0$ and $\mathbf{m}_w = \mathbf{k}$). Pressure on the left boundary is specified to be $p = 1$ and pressure on the right boundary is specified as $p = 0$. Zero flux is specified at $y = 0$ and $y = 1$. The permeability throughout the domain is uniform and isotropic ($\mathbf{k} = \mathbf{I}$) except in the low permeability streak, designated in Fig. 1 by bold curves, where the permeability is specified such that the component parallel to the streak ($k_{\|}$) is equal to 0.1 and the component perpendicular to the streak ($k_{\perp}$) is equal to 0.001. The permeability within the streak (in the $x-y$ coordinate system) is therefore a full tensor quantity which varies with

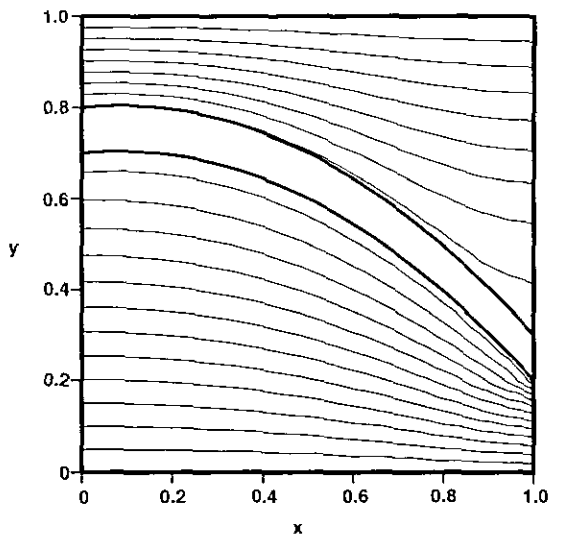

FIG. 2. Streamlines for flow through region with low permeability streak.

x. Streamlines computed from the mixed finite element solution of this problem are shown in Fig. 2. Clearly, as expected, very little fluid penetrates the low permeability region, due to the very low value of $k_{\perp}$. This simple example illustrates the ability of the triangle based mixed finite element method to accurately resolve and model the effects of irregular geometric structures with abrupt variations in permeability. Other finite element methods are less adept at handling irregular features with discontinuous properties. Finite difference methods are also ill suited for problems of this sort.

2.3. *Finite Volume Solution of the Saturation Equation*

The general method applied to the solution of the saturation equation is formulated and described in detail in [3, 4] for systems of the form of Eq. (2b). We shall concentrate here on applying this method to the more general saturation equation (1b) and in combining this approach with the solution of the pressure equation described above. As discussed in Section 1, the scheme entails a finite volume approach used in conjunction with a triangle based adaptive stencil to obtain a higher-order accurate approximation for S_w. As demonstrated in [3], the scheme is in general weakly second-order accurate in the L_1 error norm for solution of hyperbolic conservation laws.

In formulating the finite volume scheme, it is useful to rewrite Eq. (1b) as follows:

$$\nabla \cdot (\mathbf{h}_w \cdot \nabla S_w) - \nabla \cdot \mathbf{F} + Q_w = \phi \frac{\partial S_w}{\partial t}, \tag{10a}$$

$$\mathbf{F} = f_w[\mathbf{v}_t + \mathbf{m}_o(\rho_w - \rho_o)\, g \cdot \nabla D]. \tag{10b}$$

Here, the flux $\mathbf{F}$ contains both convective and gravitational components. To apply the finite volume approach, we integrate Eq. (10a) over a triangular element; i.e.,

$$\frac{\partial}{\partial t}\int_{\Delta} \phi S_w \, dA = -\int_{\Delta} (\nabla \cdot \mathbf{F})\, dA + \int_{\Delta} \nabla \cdot (\mathbf{h}_w \cdot \nabla S_w)\, dA + \int_{\Delta} Q_w \, dA. \tag{11}$$

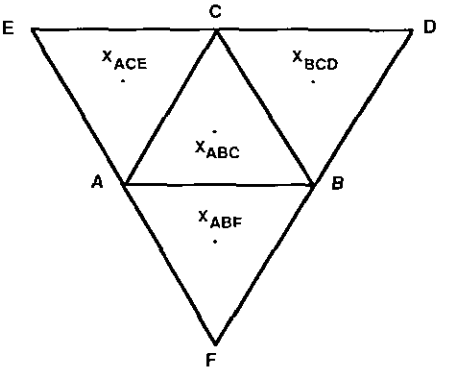

FIG. 3. Schematic of a portion of the triangular mesh.

Applying the divergence theorem and defining the element average saturation $\bar{S}_w$ as

$$\bar{S}_w = \frac{1}{|\Delta|}\int_{\Delta} S_w \, dA, \tag{12a}$$

where $|\Delta|$ is the area of the element, gives, for Δ_{ABC} (defined in Fig. 3),

$$\phi \frac{\partial \bar{S}_w}{\partial t} = -\frac{1}{|\Delta_{ABC}|}\left[\int_{l_{AB}} (\mathbf{F} - \mathbf{h}_w \cdot \nabla S_w)\cdot \mathbf{n}_{AB}\, dl + \int_{l_{AC}} (\mathbf{F} - \mathbf{h}_w \cdot \nabla S_w)\cdot \mathbf{n}_{AC}\, dl + \int_{l_{BC}} (\mathbf{F} - \mathbf{h}_w \cdot \nabla S_w)\cdot \mathbf{n}_{BC}\, dl\right], \tag{12b}$$

where we have, for now, neglected the source term.

We first consider the approximation of the convective terms. The convective flux is designated J_c; i.e.,

$$J_c = \int_{l_{AB}} \mathbf{F}\cdot\mathbf{n}_{AB}\, dl + \int_{l_{AC}} \mathbf{F}\cdot\mathbf{n}_{AC}\, dl + \int_{l_{BC}} \mathbf{F}\cdot\mathbf{n}_{BC}\, dl. \tag{13a}$$

From Eq. (10b), it is evident that the convective flux terms contain contributions from the total velocity field and from gravitational effects. In many cases, the $\mathbf{v}_t$ terms constitute the dominant contribution to the flux function $\mathbf{F}$. These terms enter the formulation via integrals over the element edges; i.e., through integrals of the form

$$\int_l f_w(\mathbf{v}_t \cdot \mathbf{n})\, dl. \tag{13b}$$

In Section 2.2, it was indicated that the mixed finite element solution of the pressure equation yields superconvergent fluxes (i.e., $O(l^2)$ accurate) at edge midpoints. Integrals of the normal component of $\mathbf{v}_t$ over element edges are likewise $O(l^2)$ accurate. Thus, because the integrals in Eq. (13b) involve $\mathbf{v}_t$ in precisely this form, the total velocity field is incorporated into the finite volume solution of the saturation equation in an optimal fashion. Alternate finite element schemes for the solution of the saturation equation, which use $\mathbf{v}_t$ directly rather than $\mathbf{v}_t \cdot \mathbf{n}$ integrated over an element edge, do not optimally utilize the mixed finite element solution of the pressure equation.

A semi-discrete approximation of the element average saturation, where $u \approx \bar{S}_w$, will be used in the solution of the saturation equation. If we designate the numerical flux across an edge (i.e., the numerical approximation to $\mathbf{F}\cdot\mathbf{n}$) as h, then a first-order accurate approximation of the convective flux can be expressed as

$$J_c = h_{AB}(u_{ABC}, u_{ABF})\cdot l_{AB} + h_{AC}(u_{ABC}, u_{ACE})\cdot l_{AC} + h_{BC}(u_{ABC}, u_{BCD})\cdot l_{BC}, \tag{13c}$$

where h_{AB} is the numerical flux across edge AB and l_{AB} is the length of edge AB.

A higher-order accurate approximation for J_c is desirable to minimize numerical dispersion. To generate such an approximation, it is necessary to express the element average data in terms of piecewise linear approximations for u. Further, these piecewise linear approximations for u must be formed in conjunction with slope limiters to avoid the introduction of any spurious oscillations into the numerical solution. The linear function approximating u in Δ_{ABC} is designated L_Δ. In any interior element, three candidates for L_Δ, designated L_Δ^i, are formed; i.e.,

$$L_\Delta^i = a_i x + b_i y + c_i. \tag{14}$$

These linear approximations involve only adjacent elements and, in all cases, the element average of L_Δ^i for Δ_{ABC} is equal to u_{ABC}. The first such candidate, L_Δ^1, is the linear interpolant of the three values

$$(\mathbf{x}_{ABC}, u_{ABC}), (\mathbf{x}_{BCD}, u_{BCD}), (\mathbf{x}_{ACE}, u_{ACE}),$$

L_Δ^2 is the interpolation of

$$(\mathbf{x}_{ABC}, u_{ABC}), (\mathbf{x}_{BCD}, u_{BCD}), (\mathbf{x}_{ABF}, u_{ABF}),$$

and L_Δ^3 the interpolation of

$$(\mathbf{x}_{ABC}, u_{ABC}), (\mathbf{x}_{ACE}, u_{ACE}), (\mathbf{x}_{ABF}, u_{ABF}),$$

where we have assumed that no three of the triangle centroids are colinear. These three linear interpolants are depicted in Fig. 4.

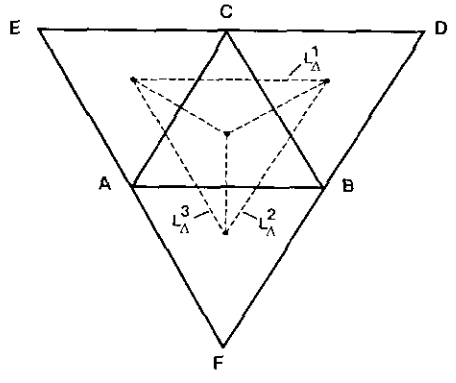

FIG. 4. Three candidates for the linear interpolation of u over Δ_{ABC}.

To select a limited version of the three possible L_Δ^i we compute the magnitude of the gradient of each L_Δ^i:

$$|\nabla L_\Delta^i| = (a_i^2 + b_i^2)^{1/2}, \tag{15}$$

for $i = 1, 2, 3$. A valid slope limiter, particularly applicable to problems involving nonlinear J_c, corresponds to the selection of the L_Δ^i for which $|\nabla L_\Delta^i|$ is the minimum. At extrema, identified when

$$u_{ABC} > \max[u_{ACE}, u_{BCD}, u_{ABF}]$$

or

$$u_{ABC} < \min[u_{ACE}, u_{BCD}, u_{ABF}],$$

a first-order approximation ($L_\Delta = u_{ABC}$) is used. This scheme will not generally introduce any spurious oscillations into the numerical solution. However, the scheme as described cannot be proven to obey a local maximum principle. A slightly more complex version of the limiting procedure, developed in [4], was proven to satisfy a local maximum principle. This modified scheme requires that additional tests on the L_Δ^i be performed to assure that L_Δ^i evaluated at the midpoints of the edges of Δ_{ABC} is not an extrema relative to u in any of the elements that share a common point with Δ_{ABC}. Rather than actually perform this test, which can be somewhat involved for irregular triangulations, we simply assure that L_Δ^i, evaluated at the edge midpoints, not introduce any new extrema globally. This approach is simpler to implement and assures that the scheme satisfies a global maximum principle. The limiter described above is applicable to nonlinear flux functions. A more compressive limiter, applicable to linear flux functions, is described in detail in [3].

At this point we can form a second-order accurate expression for J_c. For any edge, specifically edge AB, we designate $\mathbf{x}_{AB}$ to be the midpoint of the edge and $L_\Delta(\mathbf{x}_{AB}^i)$ to be the limit of $L_\Delta(\mathbf{x})$ as $\mathbf{x} \to \mathbf{x}_{AB}$ from inside Δ_{ABC} and $L_\Delta(\mathbf{x}_{AB}^o)$ to be the limit as $\mathbf{x} \to \mathbf{x}_{AB}$ from outside Δ_{ABC}. With reference to Fig. 3, $L_\Delta(\mathbf{x}_{AB}^i)$ corresponds to L_Δ for Δ_{ABC} while $L_\Delta(\mathbf{x}_{AB}^o)$ corresponds to L_Δ for Δ_{ABF}. Now, the second-order accurate approximation for J_c is

$$\begin{aligned} J_c = {} & h_{AB}(L_\Delta(\mathbf{x}_{AB}^i), L_\Delta(\mathbf{x}_{AB}^o)) \cdot l_{AB} \\ & + h_{AC}(L_\Delta(\mathbf{x}_{AC}^i), L_\Delta(\mathbf{x}_{AC}^o)) \cdot l_{AC} \\ & + h_{BC}(L_\Delta(\mathbf{x}_{BC}^i), L_\Delta(\mathbf{x}_{BC}^o)) \cdot l_{BC}. \end{aligned} \tag{16}$$

We use the EO numerical flux as described in [3] to approximate $h(\cdot, \cdot)$. This basically entails computing $\mathbf{n} \cdot \partial \mathbf{F}/\partial S_w$ at element edges and upwinding accordingly. Additional complexity arises in the vicinity of sonic points [13]; i.e., points at which $\mathbf{n} \cdot \partial \mathbf{F}/\partial S_w = 0$. Such points can occur in simulations involving gravity effects when the two terms in Eq. (10b) are of opposite signs, as will be illustrated below. At these points, an extra contribution to the numerical flux, of the form $\mathbf{n} \cdot \mathbf{F}(S_w^*)$, where S_w^* designates the sonic point, is required. The second-order approximation for J_c is retained at sonic points.

When $\mathbf{k}$, and therefore $\mathbf{m}_o$, varies from one element to the next, and when gravitational effects are present, it is evident from Eq. (10b) that the convective flux function itself ($\mathbf{F}$) differs across element edges. It is important to emphasize that we are here referring not to the particular value of the flux function $\mathbf{F}(S_w)$, which is, of course, in general discontinuous across element edges due to the discontinuity in S_w, but to the flux function itself. The flux function is, in such cases, inconsistent. When the flux function differs in adjacent elements, some of the theoretical convergence criteria for the hyperbolic solution method are violated. In addition, from a more practical point of a view, if the flux function is inconsistent and if $\mathbf{n} \cdot \partial \mathbf{F}/\partial S_w$ changes sign between the two elements, the calculation of S_w^* and therefore the sonic point contribution to the numerical flux, are ambiguous because the sonic point differs in the two adjacent elements.

From the discussion above, it is clear that even in the absence of sonic points it is desirable that the flux function itself ($\mathbf{F}$) not differ between adjacent elements. Further, inspection of Eqs. (10b) and (13a) reveals that the continuity of the scalar quantity $\mathbf{n} \cdot \mathbf{k} \cdot \nabla D$ across element edges ensures that the numerical flux function does not change across element edges; i.e., continuity of $\mathbf{n} \cdot \mathbf{k} \cdot \nabla D$ yields a consistent numerical flux function (recall that $\mathbf{v}_t$ is continuous across element edges and that f_w is a function of S_w only). Therefore, the flux function can be rendered consistent as follows. In computing the numerical flux function at a particular edge, the arithmetic average of the scalar quantity $\mathbf{n} \cdot \mathbf{k} \cdot \nabla D$ is computed from the properties of the two adjacent elements and this average value is used in the calculations. This corresponds physically to the assumption that the permeability $\mathbf{k}$ does not change discontinuously between adjacent elements but that a transition region exists.

Use of this consistent numerical flux results in a robust technique, even in the presence of large variations in the permeability field. Other approaches, such as computing numerical fluxes for each element individually and then averaging, resulted in numerical difficulties (e.g., violation of a maximum principle) in the vicinity of sonic points in some cases. This completes the description of the second-order accurate approximation for J_c.

The approximation of the diffusive flux, designated J_d, will now be considered. From Eq. (12b) we have

$$\begin{aligned} J_d = {} & \int_{l_{AB}} (\mathbf{h}_w \cdot \nabla S_w) \cdot \mathbf{n}_{AB}\, dl + \int_{l_{AC}} (\mathbf{h}_w \cdot \nabla S_w) \cdot \mathbf{n}_{AC}\, dl \\ & + \int_{l_{BC}} (\mathbf{h}_w \cdot \nabla S_w) \cdot \mathbf{n}_{BC}\, dl. \end{aligned} \tag{17}$$

A variety of methods could be used to approximate the ∇S_w terms. The approach taken here makes use of the L_Δ already formed for the approximation of J_c. The quantity $(\mathbf{h}_w \cdot \nabla S_w) \cdot \mathbf{n}_{AB}$ can be evaluated at $\mathbf{x}_{AB}$ using L_Δ for Δ_{ABC}, designated L_Δ^{ABC}; i.e.,

$$r_{AB}^i = [\mathbf{h}_w \cdot \nabla L_\Delta^{ABC}]_{\mathbf{x}_{AB}} \cdot \mathbf{n}_{AB} l_{AB}, \tag{18a}$$

where the i superscript indicates that the quantity is evaluated inside Δ_{ABC}. The analogous quantity evaluated outside Δ_{ABC} (inside Δ_{ABF}) is

$$r_{AB}^o = [\mathbf{h}_w \cdot \nabla L_\Delta^{ABF}]_{\mathbf{x}_{AB}} \cdot \mathbf{n}_{AB} l_{AB}. \tag{18b}$$

Now, given r_{AB}^i and r_{AB}^o, the integral over l_{AB} in Eq. (17) can be estimated via the harmonic average of these two scalar quantities:

$$\int_{l_{AB}} (\mathbf{h}_w \cdot \nabla S_w) \cdot \mathbf{n}_{AB}\, dl \approx \frac{2 r_{AB}^i r_{AB}^o}{r_{AB}^i + r_{AB}^o}. \tag{19}$$

The other terms in Eq. (17) are approximated similarly. In this way, the diffusive flux J_d is formed. More accurate approximations for ∇S_w, involving all three L_Δ^i, could be formed if greater accuracy is required in the capillary pressure terms. However, because this term is generally very small compared to convective effects (i.e., $\mathrm{Pe} \gg 1$), this approximation should suffice for our purposes.

The term on the RHS of the mixed finite element representation of the pressure equation (Eq. (6b)) involving $(dp_c/dS_w)\nabla S_w$ is handled in a manner analogous to the diffusive flux terms considered above. However, in evaluating the integral in Eq. (6b), the divergence theorem is not applied. Rather, the area integral is evaluated directly. The linear function L_Δ^{ABC} is used to approximate ∇S_w over the element and also to evaluate dp_c/dS_w at the Gauss points. In this way, capillary pressure effects are included in the mixed finite element representation of the pressure equation.

The saturation equation for Δ_{ABC} can now be written in the form

$$\phi \frac{\partial \bar{S}_w}{\partial t} = -\frac{1}{|\Delta_{ABC}|}\left(J_c - J_d - \int_\Delta Q_w\, dA\right). \tag{20}$$

This equation is integrated in time via a second-order accurate ENO (essentially non-oscillatory) Runge–Kutta procedure, as described in [14]. The scheme is subject to a CFL restriction of about 0.3, where the length scale used is an element side length. As indicated earlier, the global method as described here is not formally second order accurate in time. Though global second-order time accuracy does not appear to be essential in practice (second-order spatial accuracy is clearly more important), second-order time accuracy can be accomplished through some slight modifications to the method. Specifically, the backward Euler time integration of the pressure equation can be replaced by a trapezoidal rule time integration. The second-order accurate solution of the pressure equation requires an estimate of the saturation at time $n+1$, which is not yet known at this stage of the solution procedure. S^{n+1} could, however, be approximated by a preliminary integration of the saturation equation using the velocity field at time n. Second-order accurate time integration of the saturation equation additionally requires an estimate of the velocity field at time $n+\frac{1}{2}$, which is easily accomplished via linear interpolation of the velocity fields at times n and $n+1$, both known at this stage.

In some reservoir simulation problems, if the well rates and boundary conditions are held constant for some period of time, the time scale for changes in the pressure and velocity fields can be much greater than the time scale for changes in saturation. For such cases, a multiple time-stepping procedure can be used, where the velocity field is updated less frequently than the saturation field. This approach can result in considerable computational savings, as the solution of the pressure equation is typically much more computationally intensive than is solution of the saturation equation.

This completes our description of the numerical solution of the saturation equation. Before discussing numerical results for complex two phase reservoir flow problems, we shall present some results for simple one-dimensional solutions of the saturation equation. In the example problems, no capillary pressure or source terms are included. In all cases, $\mathbf{v}_t = \mathbf{i}_x$ and the saturation at $x = 0$ is fixed to be $S_w = 1$. The fractional flow function for the first example problem corresponds to the curve labeled $G_d = 0$ in Fig. 5. This frac-

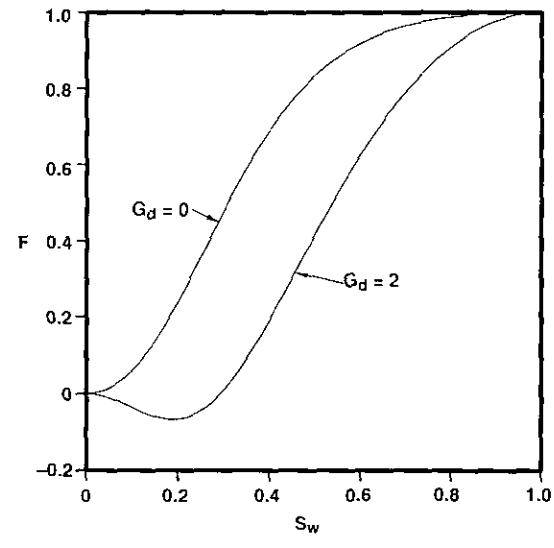

FIG. 5. Fractional flow function for two values of G_d.

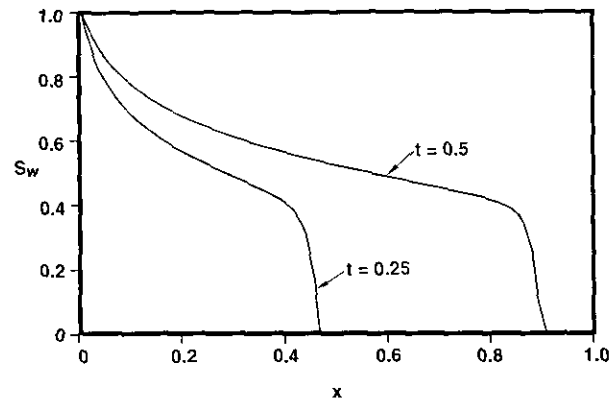

FIG. 6. Solution profiles for one-dimensional displacement with $G_d = 0$.

tional flow results from specifying $k_{rw} = S_w^2$, $k_{ro} = (1 - S_w)^2$, and $\mu_o/\mu_w = 5$, with no gravity effect. Saturation profiles at $t = 0.25$ and $t = 0.5$ are shown in Fig. 6. For this simulation, 80 triangular elements were used in the x-direction; periodic boundary conditions in y were used to simulate a one-dimensional displacement. In the figure, the solution front and the rarefaction behind the front are clearly resolved. The theoretical shock height for this problem is 0.41, which is in good agreement with the numerical results. The next case considered utilizes the fractional flow curve labeled $G_d = 2$ in Fig. 5. In this case, the flux function includes gravitational effects which act in the direction opposite to that of $\mathbf{v}_t$; i.e., in the negative x-direction. Note that this fractional flow curve contains a sonic point at $S_w = 0.19$. Saturation profiles for this case at $t = 0.25$ and $t = 0.5$ are shown in Fig. 7. At no time during the displacement do unphysical oscillations in the solution develop, even in the vicinity of the sonic point. The solution profile clearly progresses slower and displays a steeper front in this case than in the previous case, as would be expected. The theoretical shock height in this case is 0.76, again in good agreement with the numerical results.

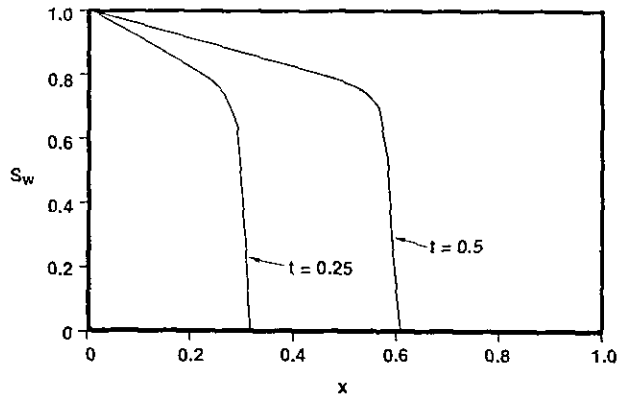

FIG. 7. Solution profiles for one-dimensional displacement with $G_d = 2$.

3. NUMERICAL EXAMPLES

In this section we apply the methodology developed in the preceding section to three example problems. Before considering these examples, however, we shall discuss some previous findings regarding the applicability and accuracy of the mixed finite element and finite volume methods for related problems. The applicability of triangle based mixed finite element methods and the limitations of standard finite difference approaches, for the modeling of flow through complex reservoir beddings was discussed in detail in [15]. There it was demonstrated that, in many cases, standard finite difference methods are unable to accurately model both reservoir geometry and permeability anisotropy simultaneously. The error incurred through use of standard finite difference approaches for the modeling of flow through inclined, anisotropic beddings was quantified for a variety of single phase flow problems and was shown to be subtantial in many cases. Analogous error would also be incurred in more complex cases, such as in the two phase flow scenarios considered in this section.

The accuracy of the finite volume approach for solution of hyperbolic conservation laws was demonstrated through several examples in [3]. Convergence studies in [3] indicated orders of accuracy in L_1 of between 1.7 and 2.0 for both linear and nonlinear flux functions. The advantages of higher order solution techniques over first-order methods, within a finite difference context, have been discussed by many investigators; see, e.g., [16, 17]. In these references it was demonstrated that, for simulations of miscible displacements, higher order methods used in conjunction with appropriate physical dispersion models act to substantially reduce grid orientation effects. These methods were further shown to yield sharper solution fronts in simulations of immiscible displacements. Because the advantages of higher order solution techniques are clear from the results of [3, 16, 17], we shall not present any results using a first-order method here.

The first problem considered in this section is a verification of the basic method, a quarter five spot simulation of a homogeneous reservoir. For this example, we take the absolute permeability $\mathbf{k}$ to be constant and isotropic; i.e., $\mathbf{k} = \mathbf{I}$. Porosity (ϕ) in this and all subsequent examples is taken to be constant; its actual numerical value is irrelevant as it serves only to nondimensionalize time. The system considered is essentially incompressible; $c_t = 10^{-6}$. No gravity effects enter this problem because the system considered is horizontal. For this example, $k_{rw} = S_w^2$, $k_{ro} = (1 - S_w)^2$, $p_c = 0$, and $\mu_o/\mu_w = 4$. Initially, $S_w = 0$ throughout the reservoir. Results are presented in terms of pore volumes injected (PVI), which is analogous to dimensionless time.

The finite element grid for this example (Fig. 8) is completely regular and contains 800 elements. Two flow scenarios are considered for this example, as depicted in

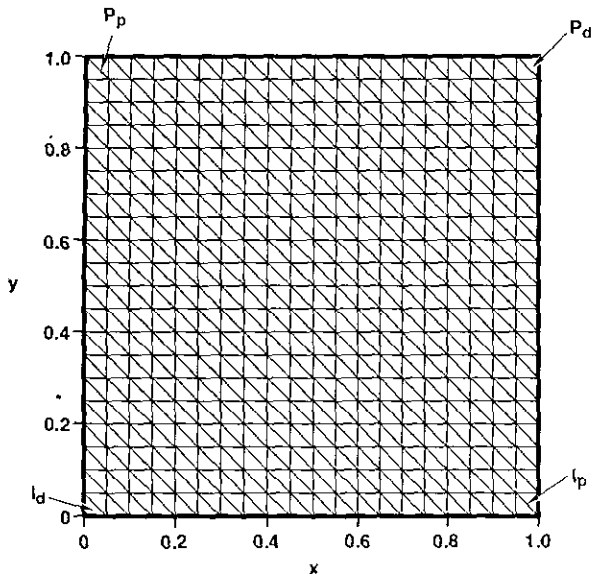

FIG. 8. Finite element grid and well arrangements for quarter five spot simulations.

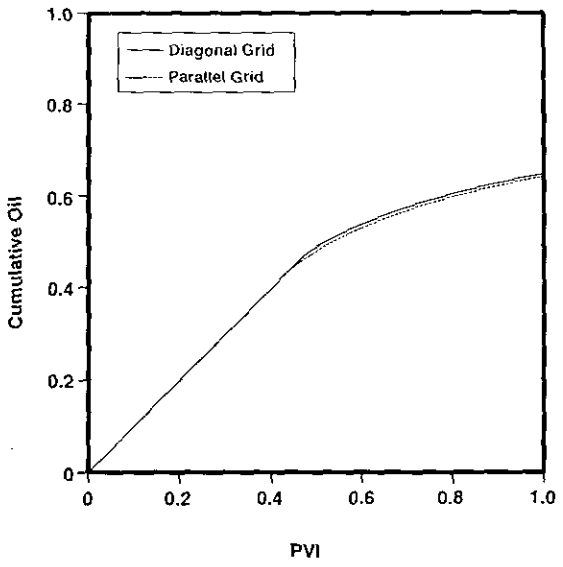

FIG. 10. Cumulative oil recovery results for diagonal and parallel flow scenarios.

Fig. 8. The first, referred to as the diagonal orientation, in analogy to the finite difference terminology, has water injection in the lower left corner of the grid (indicated as I_d in the figure) and production in the upper right corner (P_d), while the second, referred to as the parallel orientation, has injection in the lower right corner (I_p) and production in the upper left corner (P_p). Ideally, production results for these two scenarios should be identical, as the mathematical problems are themselves identical. However, due to the different numerical dispersion characteristics of the two grid orientations, simulation results will differ somewhat for the two scenarios. The extent to which these two results differ is a measure of the grid orientation effect of the method for this problem. Finite difference simulators typically display little grid orientation effect for this problem [16, 17].

Results for oil recovery (normalized by total injection) as a function of PVI are displayed in Fig. 9 for the two scenarios. There is a discernible but small difference between results for the two scenarios in this example. This discrepancy is comparable to that observed with higher order finite difference methods. Shown in Fig. 10 are results for cumulative oil recovery (i.e., pore volume of oil produced) for the two scenarios. In this display, which is typically used, the variation between the two methods appears to be minimal. Figure 11 depicts a comparison of results for oil recovery between the present method (diagonal orienta-

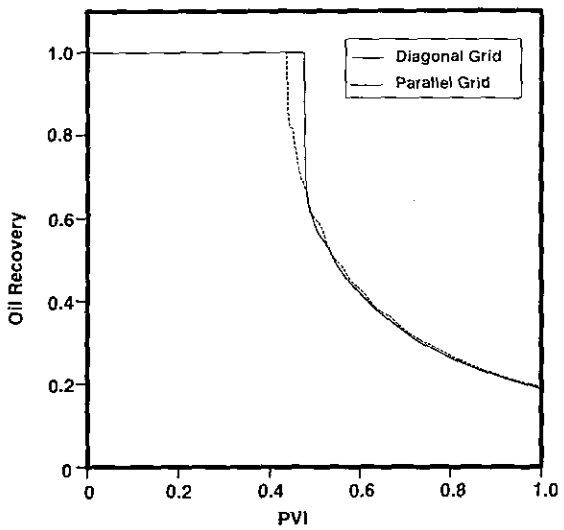

FIG. 9. Oil recovery results for diagonal and parallel flow scenarios.

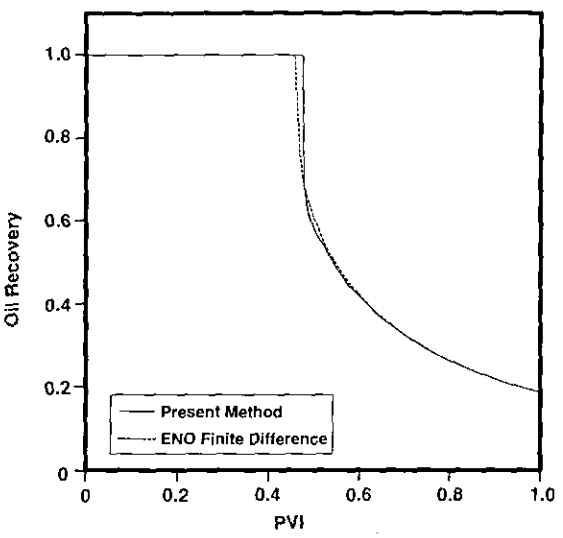

FIG. 11. Comparison of oil recovery results for present method and third-order ENO finite difference scheme.

tion) and a third-order accurate ENO finite difference scheme [17]. The ENO scheme used a 20×20 diagonal grid. The two simulation results are in excellent agreement, indicating the accuracy of the triangle based method. Results for the cumulative oil recovery predicted by the two methods are indistinguishable and are not shown.

Having demonstrated the basic accuracy of the method, we now turn to more demanding examples. The next case considered involves an irregularly shaped reservoir in the Western Overthrust Belt [18]. This particular reservoir was deposited primarily via eolian (wind-blown sand dune) processes, resulting in extensive crossbedding. This type of depositional system is particularly interesting because it can give rise to a very complex permeability field. Specifically, in addition to exhibiting complicated heterogeneity patterns, which are typically observed in reservoir rock, crossbedded strata display generally anisotropic behavior; i.e., the local permeability is a full tensor quantity (nonzero off-diagonal components). This general anisotropy is due to the complex layering of eolian strata, which is generally oriented at an angle of between 0° and 30° relative to the horizontal of the undeformed reservoir. The subsequent deformation of the reservoir can even further complicate the permeability description.

The finite element mesh for a vertical cross section of the irregularly shaped reservoir is shown in Fig. 12. The permeability field used in this example is consistent with the actual depositional system but was synthetically generated unconditionally; i.e., not conditioned to any actual data. It is thus representative rather than quantitatively descriptive of the actual permeability field. The deposition is assumed to have occurred prior to deformation, when the reservoir was horizontal. The orientation (principal direction) of the local permeability tensor in the undeformed system is assumed to be $-20°$. This orientation is consistent with the "effective" or "average" orientation of a representative portion of an eolian depositional system, as computed in [15]. The ratio of the principal values of the effective permeability tensor is taken to be 10 (with the larger component in the principal direction oriented at $-20°$), again consistent with reported data. The local permeability tensor for the actual system (deformed) was obtained by rotating the permeability in the undeformed system through an angle equal to the local dip of the reservoir. This yields a local permeability tensor oriented at $-20°$ relative to the local inclination of the reservoir. A correlated heterogeneity field

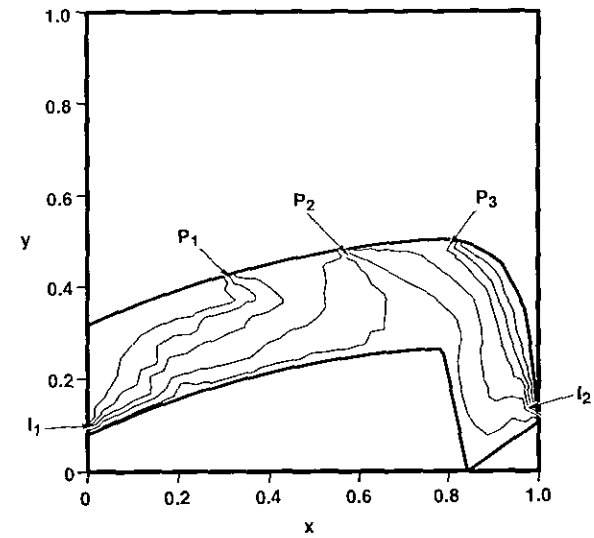

FIG. 13. Streamlines for flow through reservoir of Fig. 12 with heterogeneous and anisotropic permeability field.

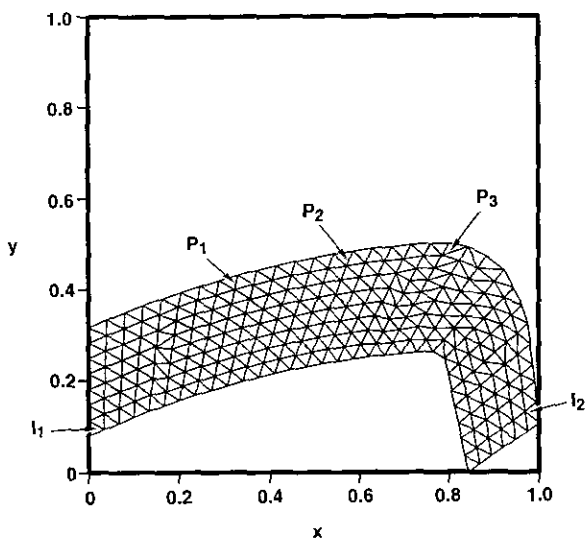

FIG. 12. Finite element mesh and well arrangements for irregularly shaped reservoir.

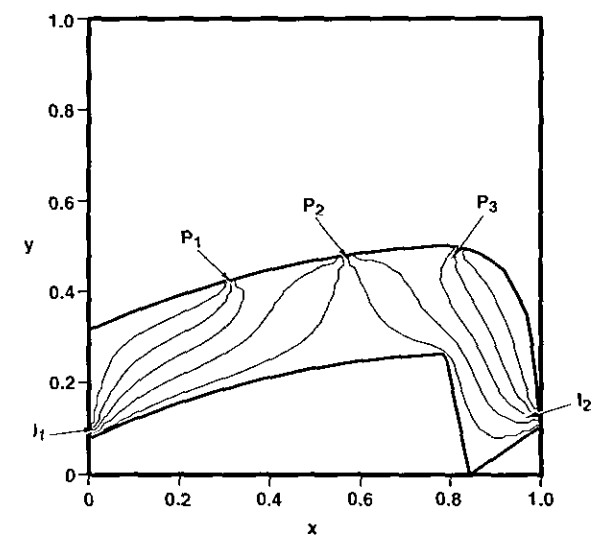

FIG. 14. Streamlines for flow through reservoir of Fig. 12 with homogeneous isotropic permeability field.

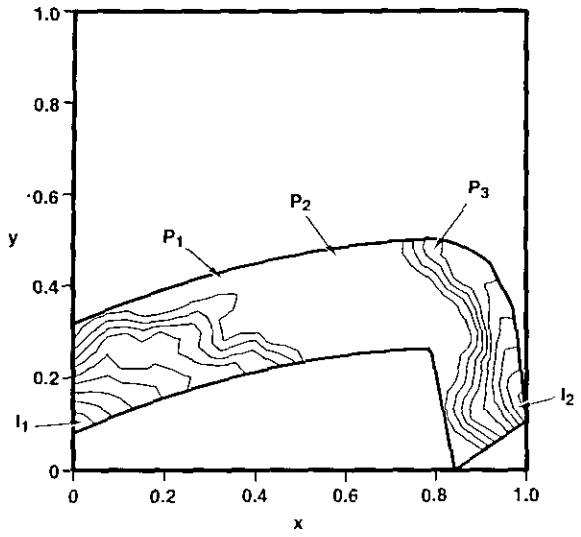

FIG. 15. Water saturation contours for two phase flow through reservoir of Fig. 12 with heterogeneous and anisotropic permeability field with $G_d = 0$.

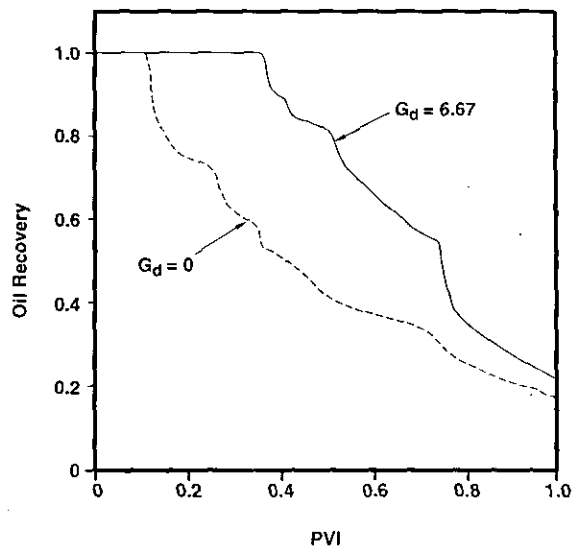

FIG. 17. Oil recovery results for flow through reservoir of Fig. 12 with heterogeneous and anisotropic permeability field.

of specified correlation length and variance is then introduced by scaling the permeability field above with a statistically isotropic scalar field of prescribed correlation length and variance, generated as described in [19]. For this example, the correlation length is taken to be 0.025 and the variance of the log of the magnitude of **k** is unity. After this scaling, the magnitude of the permeability varies by a factor of over 500 throughout the reservoir and is in general discontinuous between adjacent elements. Thus the final permeability field is quite complex, as it displays a considerable degree of heterogeneity and is generally anisotropic.

The locations of injection and production wells for this example are as indicated in Fig. 12 (this is not the production scenario of the actual reservoir). The two water injectors inject equal amounts and the three producers similarly produce equal amounts of total fluid. Because the system is essentially incompressible, total injection and total production are balanced. By varying the total injection rate, which in turn varies the dimensionless group G_d, the importance of gravitational effects (which act in the negative y-direction) relative to convective effects can be gauged. As is apparent from Figs. 6 and 7, gravitational effects can be quite significant and can act to increase the efficiency of the displacement. For this example, we take the relative permeabilities to be of the same form as above but set $\mu_o/\mu_w = 10$. We set $\rho_w = 1$ and $\rho_o = 0.8$. Again, $p_c = 0$ and $S_w = 0$ initially throughout the reservoir.

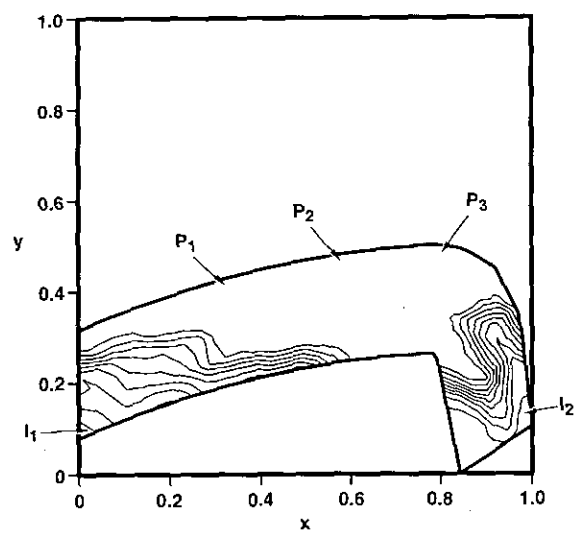

FIG. 16. Water saturation contours for two phase flow through reservoir of Fig. 12 with heterogeneous and anisotropic permeability field with $G_d = 6.67$.

The initial streamlines resulting from the well arrangement and permeability field described above are shown in Fig. 13. This flow field can be contrasted with that resulting from the same well arrangement with a homogeneous isotropic permeability description ($\mathbf{k} = \mathbf{I}$), displayed in Fig. 14. Substantial differences between the two flows are apparent, indicating the general effects of the anisotropy and heterogeneity of the permeability field. Saturation contours (ranging from $S_w = 0.1$ to $S_w = 0.9$ in increments of 0.1) for the heterogeneous case at 0.23 PVI are shown in Fig. 15. In this simulation, $G_d = 0$; i.e., no gravitational effects are present. Water breakthrough at producer P_3 has already occurred. Saturation contours at the same dimensionless time for the case $G_d = 6.67$ are shown in Fig. 16. The effect of gravity is clearly apparent in this case; the displacement is much more efficient than in the zero gravity case and water has not broken through to any of the producing wells. As discussed in Section 2.3, sonic points can occur when

gravitational effects are present. For the case considered, sonic points occur throughout the domain and at virtually every time step. Using the consistent numerical flux representation described in Section 2.3 for handling sonic point contributions in heterogeneous systems, the method encounters no difficulties in handling gravitational effects; i.e., no unphysical oscillations or spurious extrema develop. The differences between the two simulation cases are further illustrated in Fig. 17, where oil recovery as a function of PVI is plotted. The solid curve corresponds to the $G_d = 6.67$ simulation and the dashed curve to the $G_d = 0$ case. The earlier breakthrough of water in the zero gravity case clearly leads to substantially reduced oil recovery.

The last example problem considered involves simulation of two phase flow through a detailed section of an outcrop of a crossbedded eolian system. The system is identical to that of [15]; the finite element grid is shown in Fig. 18. As discussed in [15], the shaded elements correspond to so-called grainflow regions and the unshaded elements to wind ripple regions. Permeability in the grainflow regions is relatively high and isotropic; i.e., $\mathbf{k} = \mathbf{I}$ in these regions. Wind ripple regions typically display lower, anisotropic permeabilities. For these regions, we take the component of permeability in the direction parallel to the local wind ripple orientation (the local wind ripple orientation is estimated from a photograph of the outcrop; it is approximately equal to the orientation of the local grainflow strata) to be 0.3 and the component in the perpendicular direction to be 0.03.

For this example, we assign the same physical properties as in the example above. No gravitational effects are included ($G_d = 0$), though capillary pressure effects are included in this example. Capillary pressure is taken to be of the form [20],

$$p_c = A \ln \frac{S_w + \varepsilon}{1 + \varepsilon}, \tag{21a}$$

where

$$A = \frac{(p_c)_{\max}}{\ln(\varepsilon/(1+\varepsilon))}, \tag{21b}$$

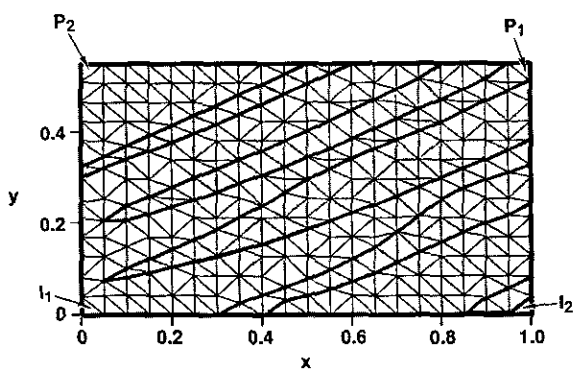

FIG. 18. Finite element mesh and well arrangements for section of eolian outcrop.

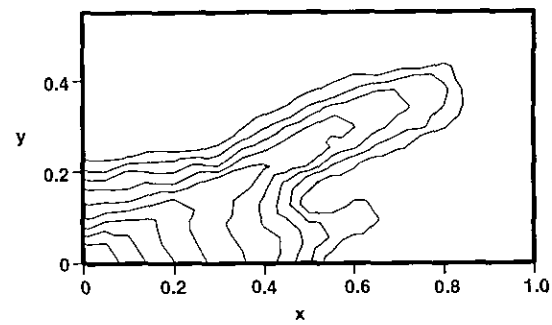

FIG. 19. Water saturation contours for two phase flow through eolian section (first flow scenario).

where ε is a parameter set to 10^{-3} and $(p_c)_{\max}$ is the maximum capillary pressure. The definition of the Peclet number [Eq. (1h)] is now

$$\mathrm{Pe} = \frac{\mu_o v_c L}{(p_c)_{\max} k_c}, \tag{21c}$$

where all quantities are as defined previously and $\bar{p}_c = (p_c)_{\max}$. In the simulation results below, the Peclet number defined in Eq. (21c) is set to 10.

Two flow scenarios are considered for this example, as depicted in Fig. 18. In the first scenario, injection is in the lower left corner (I_1) and production is in the upper right (P_1); in the second injection is in the lower right (I_2) and production is in the upper left (P_2). Saturation contours at 0.136 PVI for the first scenario are shown in Fig. 19. The displacement is quite nonuniform and clearly follows the direction of the high permeability grainflow regions and the high permeability component of the wind ripple region. Contours at the same dimensionless time for the second scenario are shown in Fig. 20. The displacement is more uniform in this case than in the first case, with the contours much less affected by the eolian features. The differences between the contours in Figs. 19 and 20 illustrate the effects of complex strata in influencing displacement processes.

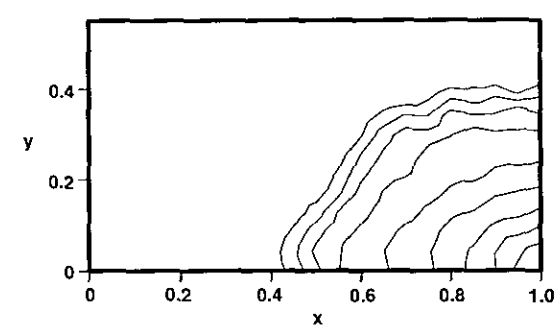

FIG. 20. Water saturation contours for two phase flow through eolian section (second flow scenario).

4. CONCLUSIONS AND POSSIBLE EXTENSIONS

The intent of this paper was to develop and apply an accurate triangle based method for the simulation of immiscible displacements in porous media. The general method combines a mixed finite element method for solution of the parabolic pressure equation with a TVD-type finite volume method for solution of the essentially hyperbolic saturation equation. As was shown in Section 2, the finite volume scheme couples optimally with the mixed finite element solution of the pressure equation, essentially because the mixed finite element method yields second-order accurate approximations for the fluxes through element edges, and these are precisely what is required by the finite volume method.

The applicability of the method for the modeling of two phase flow through geologically complex regions was demonstrated in Section 3. There it was seen that heterogeneous, generally anisotropic permeability fields can be readily modeled with the triangle based method. The effects of gravity, the importance of the permeability specification, and the influence of complex strata on immiscible displacement results were illustrated for several example cases.

Several extensions of the general method presented here would be of considerable use. The approach could be readily applied to the solution of first-contact-miscible displacement problems. For such problems, the flux function is linear and the more compressive limiter developed in [3] would be preferable to the less compressive limiter applied in this study. The methodology could also be extended to three-phase, multicomponent systems. The higher order solution of the coupled hyperbolic equations describing the multicomponent system would best be accomplished through diagonalization of the $\partial \mathbf{F}/\partial \mathbf{S}$ matrix, with each field interpolated and limited separately. The implicit solution of the saturation equation could be useful in some cases, particularly for three-phase systems with phase behavior. Higher order, fully implicit solution methods are currently being studied within a finite difference context and could eventually be applied to triangle based methods.

ACKNOWLEDGMENTS

I am grateful to W. H. Chen, M. C. H. Chien, and S. Osher for many useful discussions and suggestions.

REFERENCES

1. G. Chavent and J. Jaffre, *Mathematical Models and Finite Elements for Reservoir Simulation* (North-Holland, New York, 1986).
2. G. Chavent, G. Cohen, J. Jaffre, R. Eymard, D. R. Guerillot, and L. Weill, Discontinuous and mixed finite elements for two-phase incompressible flow, *SPE Res. Eng.* 567 (Nov. 1990).
3. L. J. Durlofsky, B. Engquist, and S. Osher, Triangle based adaptive stencils for the solution of hyperbolic conservation laws, *J. Comput. Phys.* **98**, 64 (1992).
4. X.-D. Liu, A maximum principle satisfying modification of triangle based adaptive stencils for the solution of hyperbolic conservation laws, *J. Comput. Phys.*, submitted.
5. B. Cockburn, S. Hou, and C. W. Shu, The Runge–Kutta local projection discontinuous Galerkin finite element method for conservation laws. IV. The multidimensional case, *Math. Comput.* **54**, 545 (1990).
6. K. Y. Choe and K. A. Holsapple, The discontinuous finite element method with the Taylor–Galerkin approach for nonlinear hyperbolic conservation laws, *Comput. Methods Appl. Mech. Eng.* **95**, 141 (1992).
7. P. A. Forsyth, "A Control Volume Finite Element Method for Local Mesh Refinement," Paper SPE 18415, 1989 SPE Symposium on Reservoir Simulation, Houston, Feb. 6–8.
8. L. S.-K. Fung, A. D. Hiebert, and L. X. Nghiem, Reservoir simulation with a control-volume finite-element method, *SPE Res. Eng.* 349 (Aug. 1992).
9. T. F. Russell and M. F. Wheeler, "Finite Element and Finite Difference Methods for Continuous Flows in Porous Media," in *The Mathematics of Reservoir Simulation*, edited by R. E. Ewing (SIAM, Philadelphia, 1983), p. 35.
10. R. E. Ewing, T. F. Russell, and M. F. Wheeler, "Simulation of Miscible Displacement Using Mixed Methods and a Modified Method of Characteristics," Paper SPE 12241, 1983 SPE Symposium on Reservoir Simulation, San Francisco, Nov. 15–18.
11. D. W. Peaceman, *Fundamentals of Numerical Reservoir Simulation* (Elsevier, Amsterdam, 1977).
12. L. D. Marini, An inexpensive method for the evaluation of the solution of the lowest order Raviart–Thomas mixed method, *SIAM J. Numer. Anal.* **22**, 493 (1985).
13. P. K. Sweby, High resolution schemes using flux limiters for hyperbolic conservation laws, *SIAM J. Numer. Anal.* **21**, 995 (1984).
14. C. W. Shu and S. Osher, Efficient implementation of essentially non-oscillatory shock-capturing schemes, *J. Comput. Phys.* **77**, 439 (1988).
15. L. J. Durlofsky, Modeling fluid flow through complex reservoir beds, *SPE Form. Eval.* (Dec. 1992).
16. J. B. Bell, C. N. Dawson, and G. R. Shubin, An unsplit, higher order Godunov method for scalar conservation laws in multiple dimensions, *J. Comput. Phys.* **74**, 1 (1988).
17. W. H. Chen, L. J. Durlofsky, B. Engquist, and S. Osher, "Minimization of Grid Orientation Effects through Use of Higher-Order Finite Difference Methods," Paper SPE 22887, 1991 SPE Annual Technical Conference and Exhibition, Dallas, Oct. 6–9.
18. L. E. Tillman, "Sedimentary Facies and Reservoir Characteristics of the Nugget Sandstone (Jurassic), Painter Reservoir Field, Uinta County, Wyoming, in *Petrogenesis and Petrophysics of Selected Sandstone Reservoirs of the Rocky Mountain Region*, edited by E. B. Coalson (Rocky Mountain Association of Geologists, Denver, 1989), p. 97.
19. L. J. Durlofsky, Representation of grid block permeability in coarse scale models of randomly heterogeneous porous media, *Water Resources Res.* **28**, 1791 (1992).
20. M. A. Christie, High-resolution simulation of unstable flows in porous media, *SPE Res. Eng.* 297 (Aug. 1989).